23rd ABCM International Congress of Mechanical Engineering
December 6-11, 2015, Rio de Janeiro, RJ, Brazil

# LASER CLADDING OF Fe-BASED BULK METALLIC GLASSES

**Marcos Fernandes de Carvalho**
**Piter Gargarella**
**Cláudio Shyinti Kiminami**
**Conrado Ramos Moreira Afonso**
Universidade Federal de São Carlos, Rodovia Washington Luís Km 235 – SP 310 – São Carlos – SP – Brazil
e-mails: marcosf_c@yahoo.com.br; piter@ufscar.br; kiminami@power.ufscar.br; conrado@ufscar.br

***Abstract.*** *Amorphous overspray powders of $Fe_{72}Nb_4Si_9B_{15}$ and $Fe_{43}Co_{29}Nb_4Si_5B_{19}$ (at%) bulk metallic glasses (BMG´s) obtained by spray forming were used in order to produce coatings on AISI 1020 mild steel substrate by laser cladding of the pre-placed powders. Several coatings were produced using different power densities (PD-J/mm$^2$) by means of a Yb fiber laser with total power of 2 kW. These coatings were characterized by scanning electron microscopy (SEM), X-ray diffraction (XRD) and Vickers microhardness. SEM and XRD analyses of the $Fe_{72}Nb_4Si_9B_{15}$ (at%) coating produced with a lower PD (4.0J/mm$^2$) prove its complete amorphous structure due to the high glass-forming ability (GFA) of this alloy and higher cooling rate applied during process. However, the other $Fe_{72}Nb_4Si_9B_{15}$ and $Fe_{43}Co_{29}Nb_4Si_5B_{19}$ (at%) coatings, irrespective of PD, exhibit nanocrystalline phases with the presence of Fe-α, $Fe_2B$ and FeNbB phases, depending on alloy. The coatings showed Vickers microhardness ranging from 340-1180 HV and 822-1260 HV, depending on PD, for $Fe_{72}Nb_4Si_9B_{15}$ and $Fe_{43}Co_{29}Nb_4Si_5B_{19}$ (at%) coatings, respectively, with higher values obtained for coatings with larger amount of amorphous phase.*

***Keywords:*** *Laser cladding, Fe-based bulk metallic glass, Amorphous phase, Nanocrystalline coating.*

## 1. INTRODUCTION

Bulk metallic glasses (BMGs) have been investigated due to their improved mechanical, physical and chemical properties over crystalline materials (Afonso, 2004; Balla, 2010; Greer, 2009; Wang, 2004). They exhibit excellent glass-forming ability (GFA) leading to formation of an amorphous structure with lower critical cooling rates of the order of 100 K/s (Wang, 2004). The use of BMGs is an opportunity to revolutionize the field of structural materials because their positive combination of strength, toughness, corrosion resistance and processability outside the envelope achievable using current technologies. Fe-based metallic glasses are actively being studied for industrial applications because the excellent combination of properties and low costs. Amorphous coatings of these alloys can be obtained on steel substrates, which may improve the corrosion properties of these materials in aggressive environments (Koga, 2014), such as chemical industries and oil refineries.

A technique commonly used to produce coatings is laser cladding. It is an advanced surface modification technique for production of metallurgically well-bonded coatings obtained in a controlled manner and which enables the applied material to be deposited selectively just where it is required (Vilar, 1999; Vilar, 2001; Zhang, 2011). It also makes possible the synthesis of non-equilibrium coatings due to high cooling rates involved of about $10^4$ K/s (Aghasibeig, 2012). The surface treatments through laser for advanced applications can enhance wear and corrosion resistance of materials (Gargarella, 2014) and present advantages such as reduction in operational costs and quality and finishing improvements (Maier, 1992).

The epitaxial solidification induced by the substrate (Gargarella, 2014), the high scanning speed needed in order to get higher cooling rates to avoid crystallization and the low ductility of many metallic glasses (Schuh, 2007) make difficult to produce perfect metallic glass coatings by laser cladding. Only a few works successfully produced metallic glass coatings by this method (Balla, 2010; Gargarella, 2014; Vilar, 1999; Vilar, 2001; Zhang, 2011). A systematic study of the influence of different processing parameters is needed to produce a perfect coating, free of defects, which could be further characterized to get information about the improved properties at the surface.

Considering this, the present study produced coatings of the $Fe_{72}Nb_4Si_9B_{15}$ and $Fe_{43}Co_{29}Nb_4Si_5B_{19}$ (at%) glass-former alloys on AISI 1020 mild steel substrate by laser cladding of pre-placed powders. The microstructure, phase formation and Vickers microhardness of the transversal section of single and overlapped tracks were investigated. The aim was to select parameters that allowed amorphous phase formation with minimal changes of the coating's composition while still creating a metallurgical bond with the steel substrate.

## 2. EXPERIMENTAL PROCEDURE

The $Fe_{72}Nb_4Si_9B_{15}$ and $Fe_{43}Co_{29}Nb_4Si_5B_{19}$ (at%) alloys were chosen as coating material because they exhibit good glass-forming ability (GFA) (Yanyan, 2012). The overspray powders were prepared by spray forming (Afonso, 2007), with particle size <45 µm and ranging from 20-53 µm for $Fe_{72}Nb_4Si_9B_{15}$ and $Fe_{43}Co_{29}Nb_4Si_5B_{19}$ (at%) alloys, respectively, and completely characterized by Afonso (2007). Laser cladding was carried out using the pre-placed powder method on square substrates of AISI 1020 mild steel with a size of 100 × 100 × 6 $mm^3$. Laser cladding experiments were conducted with Yb Fiber Laser (up to 2 kW) IGP in a high-purity argon gas atmosphere. The coatings precursors were prepared by placing a 0.2 mm thick layer of powder on the substrates. These layers were melted using different power (W), scanning speed (mm/s) and focal distance (mm) resulting in a variation of the power density (PD – $J/mm^2$). The microstructure of the coatings was analyzed by optical microscopy, using an Olympus PMG3 microscope, and scanning electron microscopy (SEM), with a FEI Inspect S50 and Philips XL30 FEG. The phases formed in the coatings were analyzed by X-ray diffraction (XRD) using a Siemens D5005 diffractometer and Cu-$K_\alpha$ radiation. The optical images and the penetration depth values were obtained using a laser scanning confocal microscopy (LSCM) Olympus, Lext model - 3D measuring laser microscope OLS4100. The analysis was conducted in a flat area created at the surface of the superimposed clad tracks (around 10 × 10 $mm^2$) and at their transversal cross section. The microhardness at the coatings' transversal cross section was measured with a HMV-2000 Shimadzu microhardness tester and a Vickers pyramid-shaped diamond indenter, under different loads from 0.05 (50.0 g) up to 2.0 kg.

## 3. RESULTS AND DISCUSSION

### 3.1 Effects of the laser processing parameters on coating's penetration depth

To investigate the influence of the laser processing parameters on the coatings' penetration depth in the steel substrate, several single clad tracks were produced on the AISI 1020 mild steel substrate using different power densities (PD – $J/mm^2$, Tab. 1).

Table 1. Laser processing parameters, calculated power density (PD, equation (1)), penetration depth and microhardness for the $Fe_{72}Nb_4Si_9B_{15}$ and $Fe_{43}Co_{29}Nb_4Si_5B_{19}$ (at%) single tracks.

| Composition | | | | | | | | | |
|---|---|---|---|---|---|---|---|---|---|
| $Fe_{72}Nb_4Si_9B_{15}$ (at%) | | | | | $Fe_{43}Co_{29}Nb_4Si_5B_{19}$ (at%) | | | | |
| Power (W) | Scanning speed (mm/s) | Penetration depth (± 0.2 µm) | PD ($J/mm^2$) | Hardness (HV) | Power (W) | Scanning speed (mm/s) | Penetration depth (± 0.2 µm) | PD ($J/mm^2$) | Hardness (HV) |
| 200 | 100 | 17.0 | 4.0 | 1184 ± 94 | 200 | 150 | - | 1.3 | - |
| 200 | 50 | 30.1 | 8.0 | 1060 ± 53 | 200 | 100 | - | 2.0 | - |
| 200 | 30 | 44.7 | 13.3 | 838 ± 79 | 200 | 66.7 | - | 3.0 | - |
| 200 | 10 | - | 40.0 | 826 ± 33 | 200 | 33.3 | - | 6.0 | 950 ± 124 |
| 400 | 100 | 24.0 | 8.0 | 790 ± 90 | 200 | 25.0 | 1.0 | 8.0 | 1198 ± 80 |
| 400 | 50 | 66.0 | 16.0 | 604 ± 28 | 200 | 16.7 | - | 12.1 | 1246 ± 107 |
| 400 | 30 | 96.0 | 26.7 | 601 ± 25 | 200 | 13.3 | - | 15.4 | 1162 ± 52 |
| 600 | 150 | 63.6 | 8.0 | 511 ± 85 | 200 | 10.0 | - | 20.0 | 1213 ± 93 |
| 600 | 100 | 70.0 | 12.0 | 458 ± 48 | 200 | 6.7 | - | 29.8 | 1258 ± 87 |
| 600 | 50 | 97.4 | 24.0 | 336 ± 28 | 400 | 150 | - | 2.7 | - |
| | | | | | 400 | 100 | - | 4.0 | - |
| | | | | | 400 | 66.7 | - | 6.0 | 899 ± 63 |
| | | | | | 400 | 33.3 | - | 12.0 | 846 ± 87 |
| | | | | | 400 | 16.7 | - | 24.1 | 848 ± 80 |
| | | | | | 600 | 150 | - | 4.0 | 1244 ± 94 |
| | | | | | 600 | 100 | - | 6.0 | 1104 ± 66 |
| | | | | | 600 | 66.7 | 0.5 | 9.0 | 1220 ± 76 |
| | | | | | 600 | 33.3 | 4.7 | 18.0 | 1005 ± 67 |
| | | | | | 600 | 16.7 | 5.3 | 36.1 | 822 ± 45 |

The PD calculations were carried out using equations (1) and (2).

$$PD = \frac{Power\ used}{Scanning\ speed \times Beam\ diameter} \quad (1)$$

$$Beam\ radius = W_0 \left[1 + \left(\frac{\lambda Z M^2}{\pi (W_0)^2}\right)^2\right]^{\frac{1}{2}} \tag{2}$$

where: $W_0$ is the beam radius at focal plane (100 µm), λ is the beam wavelength (1070 nm), Z is the relative distance from focal plane (4.0 and 8.0 mm, respectively, for $Fe_{72}Nb_4Si_9B_{15}$ and $Fe_{43}Co_{29}Nb_4Si_5B_{19}$ (at%)) and $M^2$ is a quality factor (22.4). The laser beam diameter obtained using equation (2) was 0.5 and 1.0 mm for $Fe_{72}Nb_4Si_9B_{15}$ and $Fe_{43}Co_{29}Nb_4Si_5B_{19}$ (at%) alloys, respectively.

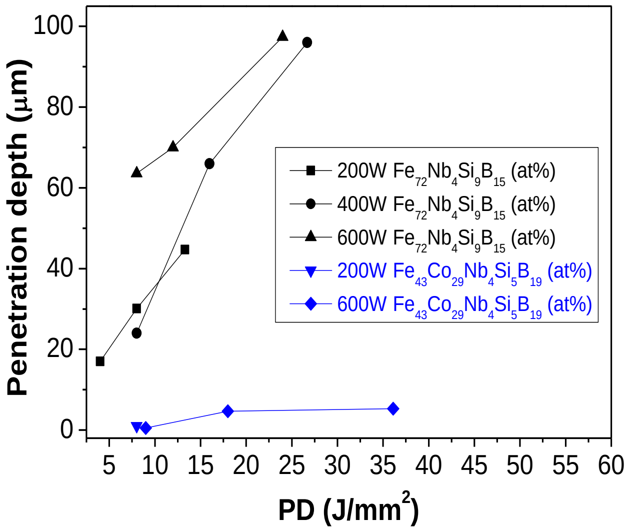


Figure 1. Variation of penetration depth at the transversal cross section of tracks in function of power density (PD) for $Fe_{72}Nb_4Si_9B_{15}$ and $Fe_{43}Co_{29}Nb_4Si_5B_{19}$ (at%) alloys, both with different laser processing parameters. As can be seen, the penetration depth increases with increasing the PD.

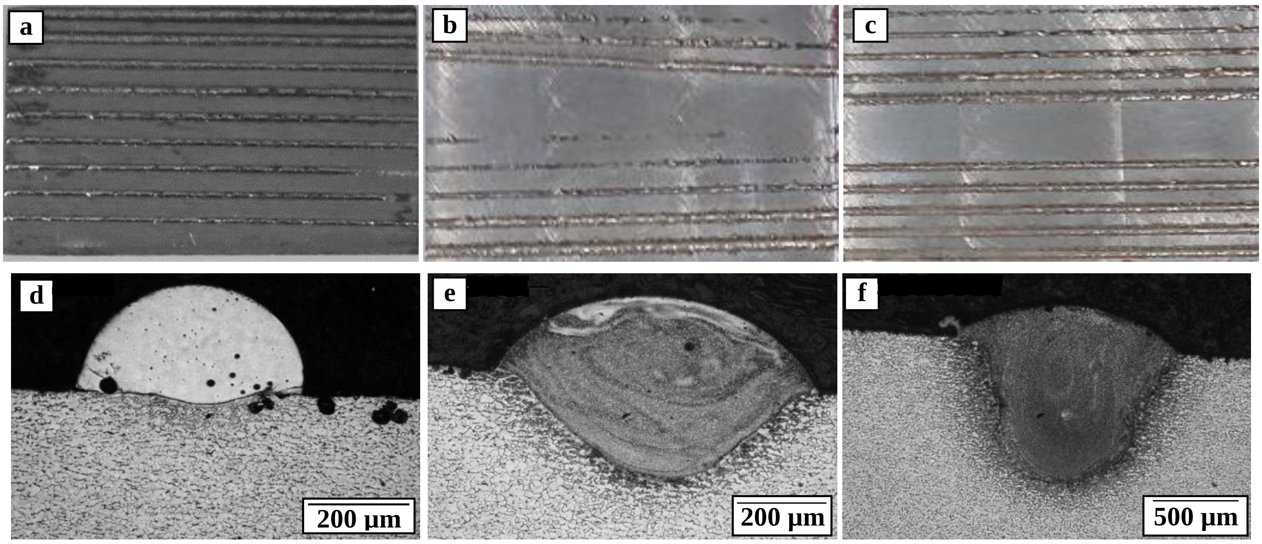


Figure 2. Digital photographs of single tracks obtained for (a) $Fe_{72}Nb_4Si_9B_{15}$ (at%) and (b)-(c) $Fe_{43}Co_{29}Nb_4Si_5B_{19}$ (at%). Optical microscopy images obtained for $Fe_{72}Nb_4Si_9B_{15}$ (at%) transversal tracks. The PDs used were (a) 4.0 J/mm², (b) 8.0 J/mm² and (c) 24.0 J/mm². It is clearly seen that penetration depth increases with increasing the PD.

Figure 1 and Table 1 show that the penetration depth increases as the PD increases, regardless of alloy, as can be seen in the optical microscopy (OM) images shown in Figs. 2 for $Fe_{72}Nb_4Si_9B_{15}$ (at%) alloy. In addition, the Figs. 2(a)-(c) show the digital photographs of single tracks obtained on the steel substrate after laser application. The OM images, Figs. 2(d)-(f) show clearly the increase in the penetration depth as the laser power increased for the same scanning speed. The penetration depth values were measured using laser scanning confocal microscopy (LSCM). These results show that a combination of lower laser power with higher scanning speed (lower PD) led to lower penetration depth of the coating material on the steel substrate, due to shorter interaction time. Figures 2(d)-(f) also demonstrates that an increase in the PD causes a decrease of the coating's height and an increase of the coating's width as expected since the energy density delivered to the power bed and substrate is reduced for lower PD.

Comparing the two alloys, Fig. 1 and Tab. 1 show that the addition of Co to the $Fe_{72}Nb_4Si_9B_{15}$ (at%) results in a significant decrease in the penetration depth, <5.3 µm. For lower PD, even no metallurgical bonding or very shallow bonding (sub-micron level) occurs for the Fe-Co-Nb-S-B composition (Tab. 1). This different behavior may be due to the higher viscosity and lower thermal conductivity of the $Fe_{43}Co_{29}Nb_4Si_5B_{19}$ (at%) alloy.

### 3.2 X-ray diffraction (XRD) analysis of the coatings

Based on the optical microscopy images and coating's penetration depth values measured using LSCM, it was observed that single tracks produced with lower PD (lower laser power and higher scanning speed) showed evidence that the coatings were in non-crystalline state or near amorphization due to its homogeneous appearance with minimal changes of the coating's composition (lower dilution and a good surface quality) while still creating a metallurgical bond with the steel substrate. These results showed that depending of laser processing parameters used, it is possible to maintain the amorphous structure after the superficial treatment of the precursor powders.

Thus, laser processing parameters used in order to produce $Fe_{72}Nb_4Si_9B_{15}$ and $Fe_{43}Co_{29}Nb_4Si_5B_{19}$ (at%) coatings, which were characterized by XRD, always resulted in lower PD. The X-ray diffractograms of the $Fe_{72}Nb_4Si_9B_{15}$ and $Fe_{43}Co_{29}Nb_4Si_5B_{19}$ (at%) coatings are presented in Figs. 3(a) and 3(b), respectively.

Figure 3(a) shows that among the $Fe_{72}Nb_4Si_9B_{15}$ (at%) coatings obtained with PDs 4.0, 8.0, 12.0 and 40.0 J/mm$^2$, all with overlapping of 0.4 mm, only the coating produced with lower PD (4.0 J/mm$^2$) exhibits a fully amorphous structure with the presence of a broad peak at 2θ = 45.0°. The parameters used to produce this coating were scanning speed of 100 mm/s, laser power of 200 W and overlapping of 0.3 %. For the other coatings, sharp Bragg peaks of the α-Fe, Reference code: 06-0696 (JCPDS, 2000), and intermetallic FeNbB (Kim, 2015) phases are seen superimposed to the broad amorphous phase peak, which also suggests the presence of amorphous phase in these coatings.

It can be concluded that the increase of PD was not favorable to the maintenance of glassy phase, therefore, the best condition to obtain coatings of $Fe_{72}Nb_4Si_9B_{15}$ (at%) with higher volume fraction of amorphous phase by laser cladding is a combination of lower laser power (200 W) and higher scanning speed (100 mm/s), i.e., lower PD.

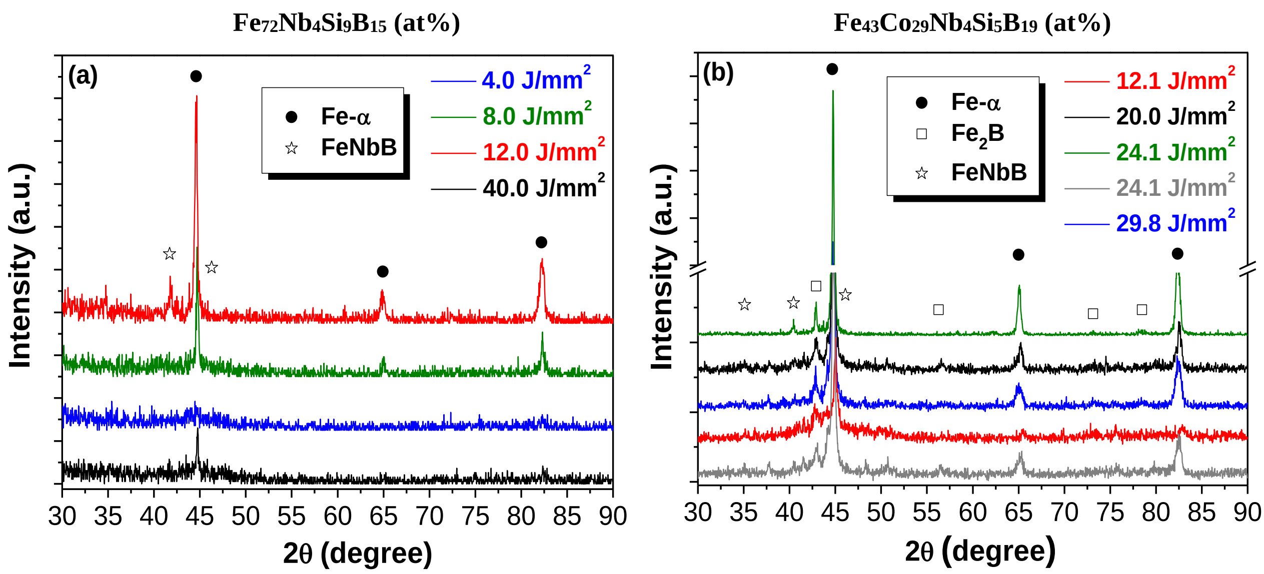


Figure 3. X-ray diffraction patters of (a) $Fe_{72}Nb_4Si_9B_{15}$ (at%) and (b) $Fe_{43}Co_{29}Nb_4Si_5B_{19}$ (at%) coatings. The power density used to produce these coatings are indicated in the Figures. The broad peak of the amorphous phase can be seen around 2θ = 45.0° for coatings produced using lower PDs.

Similar results were obtained for the $Fe_{43}Co_{29}Nb_4Si_5B_{19}$ (at%) coatings (Fig. 3(b)) produced with PDs 12.1, 20.0 and 29.8 J/mm$^2$, all with overlapping 0.5 µm and 24.0 J/mm$^2$ with overlapping 0.5 and 1.0 mm. The results show that all coatings exhibit sharp Bragg peaks of the crystalline phases α-Fe, $Fe_2B$ - Reference code: 36-1332 (JCPDS, 2000), and FeNbB (Kim, 2015) and decreasing the PD used, the amorphous phase broad peak around 2θ = 45.0° becomes clear. It can be seen that increasing B content from 15.0 to 19.0 at% was sufficient to change the phase formation through appearance of another boride phase, $Fe_2B$. These results suggest that the increase of PD was not favorable to maintenance of glassy phase, therefore, the best condition to obtain coatings of $Fe_{43}Co_{29}Nb_4Si_5B_{19}$ (at%) with higher volume fraction of amorphous phase is a lower laser power (200 W) and higher scanning speed (16.7 mm/s), i.e., lower PD.

Comparing the XRD results for both alloys, it can be seen that under the same conditions, i.e., laser power of 200 W and scanning speed 10 mm/s, the $Fe_{72}Nb_4Si_9B_{15}$ (at%) alloy (PD 40.0 J/mm$^2$, Fig. 3(a)) presented higher volume fraction of amorphous phase than $Fe_{43}Co_{29}Nb_4Si_5B_{19}$ (at%) alloy (PD 20.0 J/mm$^2$, Fig. 3(b)) indicating that Co addition difficult the maintenance of glassy phase due to  a decreasing in glass-forming ability (GFA).

The laser surface treatment of the $Fe_{72}Nb_4Si_9B_{15}$ and $Fe_{43}Co_{29}Nb_4Si_5B_{19}$ (at%) powders affected the phase formation since the phases identified in the overspray powder (without laser treatment) of $Fe_{72}Nb_4Si_{10}B_{14}$ (at%) were glassy, α-Fe, $Fe_{23}B_6$, FeB and FeNbB and for $Fe_{43}Co_{29}Nb_4Si_5B_{19}$ (at%) were glassy, $Fe_7Co_3$, $Fe_{23}B_6$, $Co_{16}Nb_6Si_7$, $(Fe,Co)_2B$ intermetallic crystalline phases (Afonso, 2007). This difference is attributed to the different cooling rates involved in the atomization and laser processing.

### 3.3 Microstructural analysis of the coatings

SEM images in backscattered electrons (BSE) mode and optical microscopy (OM) images of the transversal section of single clad tracks of the $Fe_{72}Nb_4Si_9B_{15}$ (at%) alloy are presents in Figs. 4(a)-(c), 5(a)-(c) and 6(a)-(c).

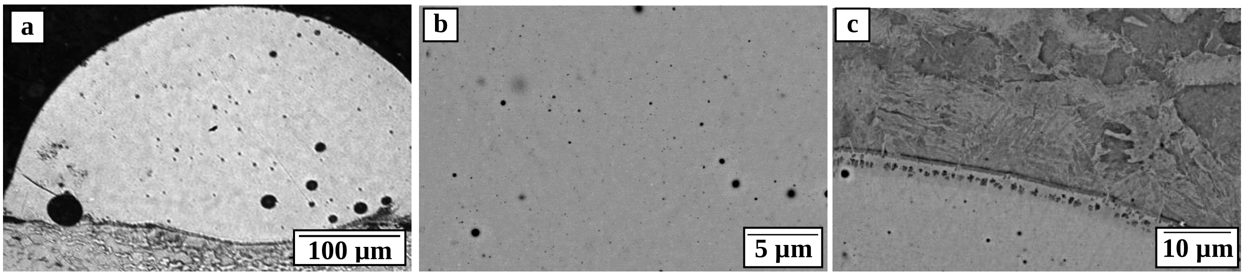


Figure 4. Transversal section of the single clad track of $Fe_{72}Nb_4Si_9B_{15}$ (at%) obtained using a laser power of 200 W and scanning speed of 100 mm/s. (a) OM image of the cross section and (b) SEM image of the clad track center and (c) of the coating/substrate interface.

The microstructures of the single clad tracks produced with lower laser power of 200 W and different scanning speeds of 100, 50 and 30 mm/s, showed that only the one produced with 100 mm/s was satisfactory, since at lower scanning speeds, the coatings presented discontinuities or high porosity due to gas entrapment during the cladding process (not shown here). The optical microscopy analysis of the single clad track produced with laser power of 200 W and scanning speed 100 mm/s showed lower penetration depth of the coating material in the steel substrate (Fig. 4(a)), and a homogeneous and without contrast microstructure, which suggests a non-crystalline state. SEM image taken at its center region confirms that no crystalline phases occur in this coating (Fig. 4(b)), indicating maintenance of glassy phase due to high GFA of this alloy. Furthermore, this result was in agreement to XRD analysis (PD 4.0 J/mm$^2$, Fig. 3(a)) where the diffractogram did not show peaks of crystalline phases, indicating high amorphous phase fraction. However, in the coating/substrate interface it is possible to see dendrites of the α-Fe phase embedded in the amorphous matrix, indicating epitaxial growth from the steel substrate (Fig. 4(c)) (Gargarella, 2014). In addition, the heat-affected zone (HAZ) formed in the substrate was narrow (5.5 µm), but it is still possible to observe a change in the gray scale of the phases as it moves up from the steel substrate to the coating.

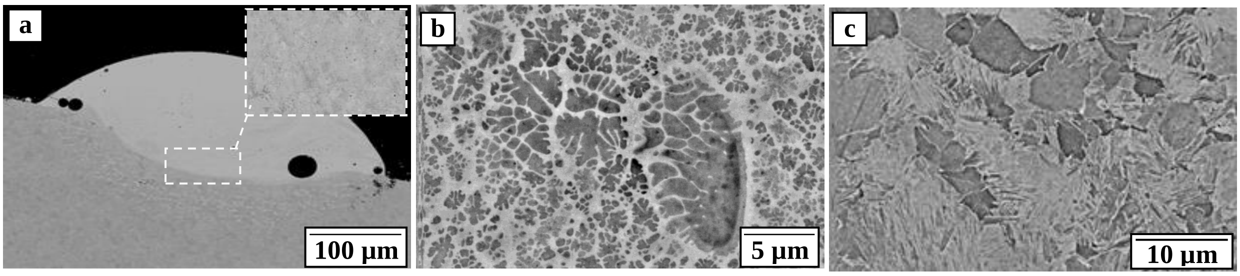


Figure 5. Typical micrographs of the transversal section of the $Fe_{72}Nb_4Si_9B_{15}$ (at%) single clad track obtained with laser power of 400 W and scanning speed of (a) 100 mm/s: clad track center, (b) 50 mm/s: with the presence of a dendritic morphology and (c) 30 mm/s: with an acicular morphology.

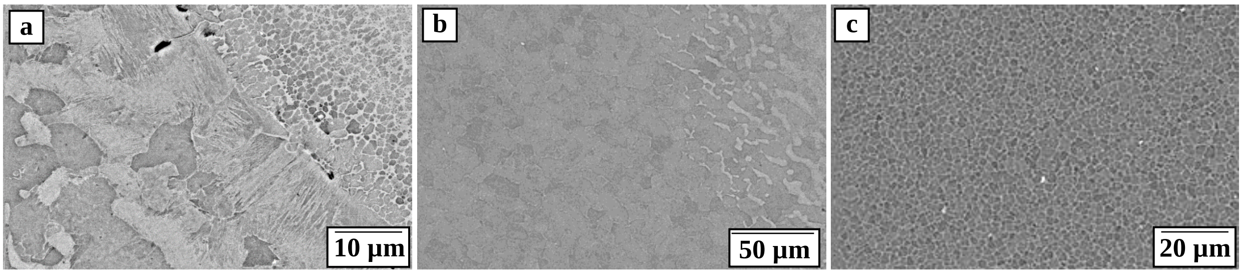


Figure 6. Typical micrographs of the transversal section of the $Fe_{72}Nb_4Si_9B_{15}$ (at%) single clad track obtained using laser power of 600 W and scanning speed of (a) 150 mm/s: coating/substrate interface, (b) 100 mm/s: dendritic morphology and (c) 50 mm/s: granular dendrite morphology.

When the laser power increased to 400 and 600 W, it was observed that more crystalline phases was formed as result of the lower cooling rate. Coatings produced with laser power of 400 W and different scanning speeds, Figs 5(a)-(c), showed that in these cases, the microstructure presented porous, small crystalline phases (FeNbB intermetallic phase) and coating/substrate interface with dendritic phases (100 mm/s, Fig. 5(a)); porous, elongated grains with columnar aspect and a coating/substrate interface with acicular morphology (50 mm/s, Fig. 5(b)) and acicular morphology (30 mm/s, Fig. 5(c)). Moreover, in the last case, the single clad track presented an imperceptible distinction of the steel substrate, indicating a very shallow bonding and lower dilution.

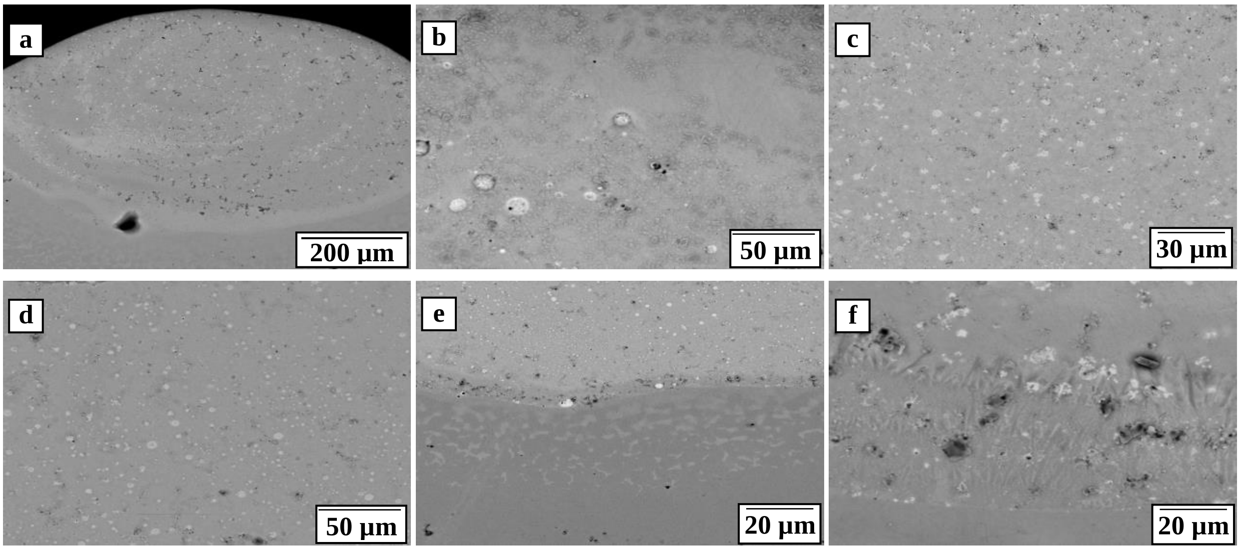


Figure 7. Typical micrographs of the single clad tracks/transversal section obtained from $Fe_{43}Co_{29}Nb_4Si_5B_{19}$ (at%) alloy.

Coatings produced with laser power of 600 W and different scanning speeds (Figs 6(a)-(c)) showed that in these cases, the microstructure presented porous, small crystalline phases (FeNbB intermetallic phases) and coating/substrate interface with dendritic phases (Figs. 6(c) and 6(b), respectively, 150 and 100 mm/s) and granular dendritic morphology (Fig. 6(c), 30 mm/s). In addition, for both cases, Figs. 5 and 6, occurred crystallization of the single clad tracks, as can be seen, FeNbB intermetallic phase appeared. The coatings presented cellular morphology and showed higher volume fraction of dendrites embedded in the amorphous matrix indicating decreasing of the amorphous phase fraction with increase of penetration depth (dilution) of the coating material on the steel substrate (Fig. 2(a)).

SEM analysis of the transversal section of single clad tracks of the $Fe_{43}Co_{29}Nb_4Si_5B_{19}$ (at%) alloy obtained with different laser processing parameters (Tab. 1) are shown in Figs. 7(a)-(f). The microstructures of the clad tracks were very similar, irrespective of laser processing parameters, and the micrographs showed that occurrence of more crystalline phases when compared to the $Fe_{72}Nb_4Si_9B_{15}$ (at%) alloy. In all cases, it was observed nanocrystalline phases (Figs. 7(a)-(f)). In addition, these results indicated that Co addition decreased the GFA comparing with $Fe_{72}Nb_4Si_9B_{15}$ (at%) for coatings produced with the same parameters. Figure 7(a) shows that the coating presented small bright phases, which correspond to the nanocrystalline FeNbB intermetallic and small dark phases, which correspond to the nanocrystalline $Fe_2B$ intermetallic. Figures 7(b)-(d) show high magnification images of the nanocrystalline FeNbB intermetallic phases embedded in the amorphous matrix. It can be seen in Fig. 7(e) a transition between clad track and steel substrate through the HAZ. In addition, the coatings exhibited an excellent interfacial bonding with the steel substrate. Finally, Fig. 7(f) shows the dendritic epitaxial growth in the coating/substrate interface.

### 3.4 Vickers microhardness measurements of coatings

Figures 8(a)-(b) show the variation Vickers microhardness values and penetration depth in the steel substrate versus PD obtained at the transversal cross section of clad tracks of $Fe_{72}Nb_4Si_9B_{15}$ and $Fe_{43}Co_{29}Nb_4Si_5B_{19}$ (at%) coatings, both with different laser processing parameters (Tab. 1).

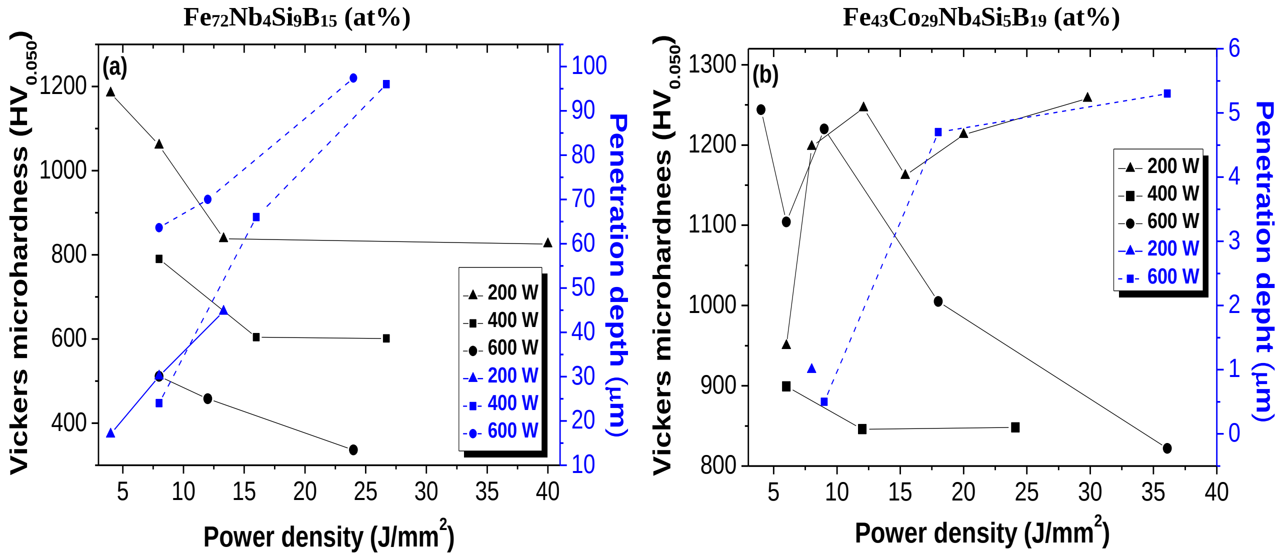


Figure 8. Variation of Vickers microhardness at the transversal cross section of tracks and penetration depth in function of power density (PD) of (a) $Fe_{72}Nb_4Si_9B_{15}$ (at%) and (b) $Fe_{43}Co_{29}Nb_4Si_5B_{19}$ (at%).

For the $Fe_{72}Nb_4Si_9B_{15}$ (at%) alloy (Fig. 8(a)) it was observed that the Vickers microhardness increased as PD and penetration depth decreased, for the same laser power. In addition, the Vickers microhardness values decreased as the laser power applied increased due to high penetration depth, which makes that more material of the metal base melts with the coating, changing its properties. Therefore, it was observed that the higher Vickers microhardness values were obtained with the lower laser power, 200 W. According to the results obtained by SEM and XRD analyses, it was observed higher volume fraction of amorphous phase for these coatings. It must be stressed that the greater the volume fraction of amorphous phase formed, in general, higher the hardness of the coatings (Gargarella, 2014).

For the $Fe_{43}Co_{29}Nb_4Si_5B_{19}$ (at%) alloy, it was not observed the same tendency as the $Fe_{72}Nb_4Si_9B_{15}$ (at%). Figure 8(b) shows that, in general, Vickers microhardness values measured were constant, according to standard deviation, irrespective laser processing parameters, except for lower PDs, 4.0, 6.0 and 9.0 J/mm$^2$ with laser power of 600 W and PD 6.0 J/mm$^2$ with laser power of 200 W. Therefore, it was observed that the higher Vickers microhardness values were obtained for coatings produced with laser power of 200 W, irrespective of scanning speed, and laser power of 600 W for small PDs, according to standard deviation. These results showed that Co addition and the increase in the B content (Yao, 2012) in the alloy composition, increased the Vickers microhardness values of the coatings produced with the same laser processing parameters. However, for laser power of 200 W, where higher volume fraction of amorphous phases was observed, the Vickers microhardness values of the coatings, in general, were the same, according to standard deviation. Also, the higher microhardness values observed for the transversal cross section of clad tracks for $Fe_{43}Co_{29}Nb_4Si_5B_{19}$ (at%), was probably due to appearance of boride phase, $Fe_2B$, which can increase its microhardness.

## 4. CONCLUSION

It was possible conclude from the studies made with the $Fe_{72}Nb_4Si_9B_{15}$ and $Fe_{43}Co_{29}Nb_4Si_5B_{19}$ (at%) alloys that coatings of these alloys with higher volume fraction of amorphous phases were produced on the AISI 1020 steel substrate by laser cladding, using lesser PD, i.e., lower laser power of 200 W with higher scanning speed of 100 mm/s. The $Fe_{43}Co_{29}Nb_4Si_5B_{19}$ (at%) coatings presented lower penetration depth than $Fe_{72}Nb_4Si_9B_{15}$ (at%) coatings due to increase of B content and Co addition. However, for both alloys, the coating's penetration depth and width increased while coating's height decreased with increasing of PD.

XRD analysis showed that only the coatings produced with lower PD exhibits a fully amorphous structure with the presence of a broad peak at 2θ = 45.0° for $Fe_{72}Nb_4Si_9B_{15}$ (at%) and broad peak + α-Fe phase for $Fe_{43}Co_{29}Nb_4Si_5B_{19}$

(at%) coatings. For other $Fe_{72}Nb_4Si_9B_{15}$ (at%) coatings, increasing PD, sharp Bragg peaks of the α-Fe and FeNbB intermetallic phases was observed while for $Fe_{43}Co_{29}Nb_4Si_5B_{19}$ (at%) coatings was observed the same phases and also $Fe_2B$, due to increase in B content. It can be concluded that the increase of PD was not favorable to the maintenance of glassy phase for $Fe_{72}Nb_4Si_9B_{15}$ and $Fe_{43}Co_{29}Nb_4Si_5B_{19}$ (at%) coatings.

SEM micrographs showed that, only with lower PD, a homogeneous and without contrast microstructure, which suggests a non-crystalline state. In addition, SEM results indicated that Co addition and increase of B content decreased the GFA of the alloy for coatings produced with the same parameters.

The Vickers microhardness values, in general, decreased as PD increased, except to $Fe_{43}Co_{29}Nb_4Si_5B_{19}$ (at%) coatings produced with laser power of 200 and 400 W. Also, the higher microhardness values were observed for $Fe_{43}Co_{29}Nb_4Si_5B_{19}$ (at%), probably due to appearance of boride phase, $Fe_2B$, which can increase its microhardness.

The aim was reached and the parameters that allowed amorphous phase formation with minimal changes of the coating's composition while still creating a metallurgical bond with the steel substrate were lower laser power, 200 W, regardless of alloy, with higher scanning speed, 100 mm/s.

## 5. ACKNOWLEDGEMENTS

The authors gratefully acknowledge the financial support of the Brazilian institutions FAPESP (São Paulo State Research Foundation) Pos-doctoral Grant (2014/13432-9) and Research Project 2012/18429-0.

## 6. REFERENCES

Aghasibeig, M., Fredriksson, H., 2012. "Laser cladding of a ferrous iron-based alloy". *Surface & Coatings*, Vol. 209, p. 32.

Afonso, C.R.M., 2004. *Conformação por spray de ligas amorfizáveis a base de ferro com característica de magnetos moles*. Ph.D. thesis, Universidade Federal de São Carlos, Brazil.

Afonso, C.R.M., Bolfarini, C., Filho, W., Kiminami, C.S., 2007. "Spray forming of glass former $Fe_{63}Nb_{10}Al_4Si_3B_{20}$ alloy". *Materials Science & Engineering. A, Structural Materials: Properties, Microstructure and Processing*, Vols. 449-451, p.884.

Balla, V.K., Bandyopadhyay, A., 2010. "Laser processing of Fe-based bulk amorphous alloy". *Surface & Coatings Technology*, Vol. 205, p. 2661.

Gargarella, P., Almeida, A., Vilar R., Afonso, C.R.M., Peripolli, S., Rios, C.T., Bolfarini, C., Botta, W.J., Kiminami, C.S., 2014. "Formation of Fe-based glassy matrix composite coatings by laser processing". *Surface & Coatings*, Vol. 240, p. 336.

Greer, A.L., 2009. "Metallic glasses…on the threshold". Materials Today, Vol. 12, p. 14.

Joint Committee on Powder Diffraction Standards, JCPDS, Powder Diffraction File – PDF-2. Database Sets 1–49, ICDD, Pennsylvania, 2000 (CDROM).

Kim, J.T., Hong, S.W., Park, H.J., Kim, Y.S., Park, G.H., Park, J.Y., Lee, N., Seo, Y., Park, J.M., Kim, K.B., 2015. "Improving tha plasticity and strength of Fe-Nb-B ultrafine eutectic composite". *Materials and Design*, Vol. 76, p. 190.

Koga, G.Y., Nogueira, R.P., Roche, V., Yavari, A.R., Melle, A.K., Gallego, J., Bolfarini, C., Kiminami, C.S., Botta, W.J., 2014. "Corrosion properties of Fe-Cr-Nb-B amorphous and coatings". *Surface & Coatings*, Vol. 254, p. 238.

Maier, C., Schaaf, P., Gonser, U., 1992. "Calculation of the temperature profile for laser treatment metallic samples". *Materials Science and Engenieering A*, Vol. 150, p. 271.

Schuh, C.A., Hufnagel, T.C., Ramamurty, U., 2007. "Mechanical bahavior of amorphous alloys". *Acta Materilia*, Vol. 55, p. 4067.

Vilar, R., 1999. "Laser alloying and laser cladding". *Materials Science Forum*, Vol. 301, p. 229.

Vilar, R., 2001. "Laser Cladding". *International Journal of Powder Mettalurgy*, Vol. 37, p. 31.

Wang, H.W., Dong, C., Shek,. C.H., 2004. "Bulk metallic glasses". *Material Science and Engennireng: R: Reports*, Vol. 44, p. 45.

Yanyan, Z., Zhuguo, L., Jian, H., Min, L., Ruifeng, L., Yixiong W., 2012. "Amorphous strucutre evolution of high power diode laser cladded Fe-Co-B-Si-Nb coatings". *Applied Surface Science*, Vol. 261, p. 896.

Yao. J.H., Hoster, C., Music, D., Frisk, A., Bjorck, M., Schneider, J.M., 2012. "Synthesis and mechanical properties of Fe-Nb-B thin-film metallic glasses". *Scripta Materialia*, Vol. 67, p. 181.

Zhang, P., Yan, H., Yao, C., Li, Z., Yu, Z., Xu, P., 2011. "Synthesis of Fe-Ni-B-Si-Nb amorphous and crystalline composite coatings by laser claddin and remelting". *Surface & Coatings*, Vol. 206, p. 1229.

## 7. RESPONSIBILITY NOTICE

The authors are the only responsible for the printed material included in this paper.